Did the 1999 earthquake swarm on Gakkel Ridge open a volcanic conduit? A detailed teleseismic data analysis

Carsten Riedel, Vera Schlindwein

▶ **To cite this version:**

Carsten Riedel, Vera Schlindwein. Did the 1999 earthquake swarm on Gakkel Ridge open a volcanic conduit? A detailed teleseismic data analysis. Journal of Seismology, 2009, 14 (3), pp.505-522. 10.1007/s10950-009-9179-6 . hal-00537995

HAL Id: hal-00537995
https://hal.science/hal-00537995

Submitted on 20 Nov 2010

HAL is a multi-disciplinary open access archive for the deposit and dissemination of scientific research documents, whether they are published or not. The documents may come from teaching and research institutions in France or abroad, or from public or private research centers.

L'archive ouverte pluridisciplinaire **HAL**, est destinée au dépôt et à la diffusion de documents scientifiques de niveau recherche, publiés ou non, émanant des établissements d'enseignement et de recherche français ou étrangers, des laboratoires publics ou privés.

J Seismol (2010) 14:505–522
DOI 10.1007/s10950-009-9179-6

ORIGINAL ARTICLE

Did the 1999 earthquake swarm on Gakkel Ridge open a volcanic conduit? A detailed teleseismic data analysis

Carsten Riedel · Vera Schlindwein

Received: 19 February 2009 / Accepted: 2 November 2009 / Published online: 20 November 2009
© Springer Science + Business Media B.V. 2009

Abstract In 1999, a seismic swarm of 237 teleseismically recorded events marked a submarine eruption along the Arctic Gakkel Ridge, later on also analyzed by sonar, bathymetric, hydrothermal, and local seismic studies. We relocated the swarm with the global location algorithm HYPOSAT and analyzed the waveforms of the stations closest to the events by cross-correlation. We find event locations scattered around 85°35′ N and 85° E at the southern rift wall and inside the rift valley of the Gakkel Ridge. Waveforms of three highly correlating events indicate a volumetric moment tensor component and highly precise referenced double-difference arrival times lead us to believe that they occur at the same geographical position and mark the conduit located further southeast close to a chain of recently imaged volcanic cones. This result is supported by station residual anomalies in the direction of the potential conduit. Seismicity is focused at the crust–mantle boundary at 16–20 km depth, but ascending toward the potential conduit during the beginning of April 1999, indicating an opening of the vent.

Keywords Gakkel Ridge · HYPOSAT · Relocation · Station residuals · Spatiotemporal organization · 1999 swarm · Polar research · Double difference · Cross-correlation · Magma ascent · Oden volcano · Ultraslow-spreading ridge

C. Riedel (✉) · V. Schlindwein
Alfred-Wegener-Institut für Polar- und Meeresforschung, Am alten Hafen 26, 27568, Bremerhaven, Germany
e-mail: carsten.riedel@awi.de

Present Address:
C. Riedel
KGS Rastede, WIlhelmstr. 5,
26180 Rastede, Germany

1 Introduction

The Arctic Gakkel Ridge (Fig. 1) is one of the slowest-spreading zones of the Earth's lithosphere (Dick et al. 2003) with a full spreading rate lower than 1.2 cm/year. Along the rift axis, volcanic and amagmatic units alternate (Michael et al. 2003). Details of the active rifting processes are still unknown due to the remote location of Gakkel Ridge and its cover with Arctic sea ice which only few research vessels can tackle. However, in 1999, a sequence of earthquakes of body wave magnitude 3.3 (International Seismological Centre [ISC]) and higher was recorded worldwide (Müller and Jokat 2000; Tolstoy et al. 2001), which is so far the largest teleseismically recorded earthquake swarm at any mid-ocean ridge (MOR) volcanic system and occurred in the area surrounding 85°40′ N, 85° E (Fig. 1). Global centroid moment tensor solutions with large isotropic components

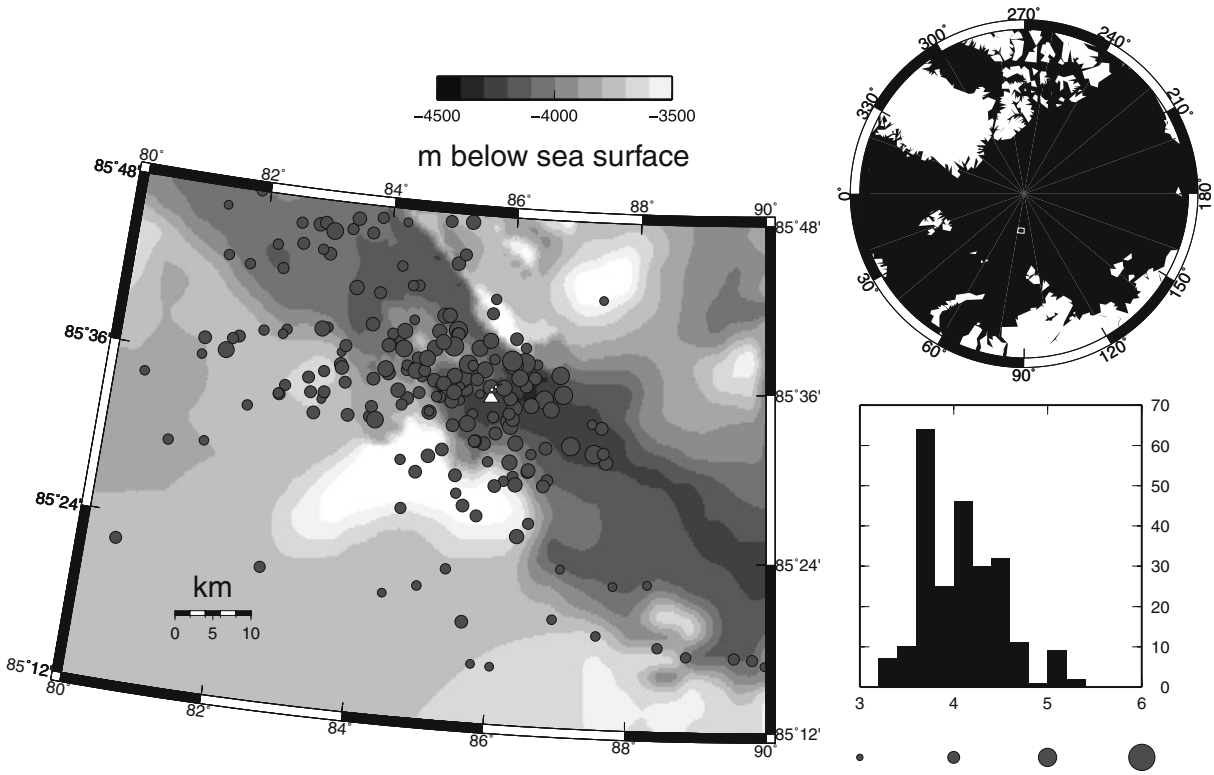

Fig. 1 The ISC locations of the 237 events mentioned in the text have been plotted as *dark gray circles* on a bathymetric map of Gakkel Ridge in the survey area on the *left side of the figure*. A scale for the bathymetry where *black* is related to topographic lows and *white* is related to topographic highs is displayed at the top. On the *right side* the position of the swarm area is marked as a *white box* on a plot of the high latitudinal areas of the northern hemisphere. Below, a histogram of magnitudes is presented. The size of the circles in the location graph is proportional to the square values of magnitude (scale see below magnitude distribution) to ease the view of high-magnitude events. A *small white triangle* (volcano) marks the position of the crater of Oden volcano which was discovered by Sohn et al. (2008). All figures including this one have been plotted using Generic Mapping Tools (Wessel and Smith 1998)

and high *b* values indicated a typical volcanic character (Müller and Jokat 2000) and sonar images from the USS Hawkbill only 4 months after the main activity showed areas of high backscatter interpreted as fresh lava flows (Edwards et al. 2001).

During the joint AMORE 2001 cruise on the USCGC Healy and RV Polarstern rock sampling, bathymetric surveys and hydrothermal studies discovered that the seismically active area represents a major volcanic complex (Michael et al. 2003). A giant hydrothermal plume in the water column indicated sustained volcanic activity (Edmonds et al. 2003; Baker et al. 2004). A local seismic experiment with seismic arrays on ice floes recorded a swarm of sea bottom explosive signals (Schlindwein et al. 2005; Schlindwein and Riedel 2009) even 2 years after the major earthquake swarm. In 2007, the AGAVE cruise revealed thick blankets of volcaniclastic sediments in the area which contain Limu o Pele, i.e., very thin glassy crystallized rims of gas bubbles in magma and, thus, clear evidence for considerable explosive volcanism at water depths of about 4,000 m and a chain of small volcanic peaks with Oden volcano (white triangle in Fig. 1) at its easternmost location (Sohn et al. 2008).

While MOR volcanism is generally considered to be effusive, the relevance of explosive eruptions at MORs has only recently been recognized (Clague et al. 2008). Understanding the seismo-volcanic episode at the 85° E volcanic complex

at Gakkel Ridge may, therefore, yield valuable new information on deep submarine eruption processes. In this light, we intensively analyze the teleseismically recorded earthquake swarm of 1999, relocating it with an advanced classical location tool, HYPOSAT, using various velocity models and exploring new ways of describing the dataset in terms of its spatiotemporal organization.

2 Dataset

We used all seismic events between January and September 1999 registered in the ISC online bulletins (we downloaded them on the 6 September 2007 from http://www.isc.ac.uk) in an area from 85° N to 87° N and 70° E to 95° E. This dataset is not completely identical to previous studies (Müller and Jokat 2000; Tolstoy et al. 2001), which used a preliminary dataset available at that time. Our dataset contains 237 events in contrast to 252 events of Tolstoy et al. (2001) with body wave magnitudes (m_b) between 3.3 and 5 (Fig. 1).

The original dataset was located using ISCloc in the ISC standard procedures as outlined in Storchak (2006) using the Jeffreys–Bullen travel time tables and a complicated weighting scheme that delivers unrealistically small errors. The root mean square (rms) travel time residual for the original dataset is ~1.14 s with only four of these events not fixed in depth.

For further analysis, we also inspected publicly available waveforms of the nearest stations that recorded the events (see Fig. 2), taking care to realize an equiazimuthal coverage. This set of waveforms includes data from the North Atlantic sector (Kings Bay [KBS], Spitsbergen array [SPITS], Daneborg–Greenland [DAG], North Norway [ARCES], and Lovozero–European Russia [LVZ]), the North American sector (Alaska array [ILAR], Inuvik-Canada [INK], and Yellowknife array–Canada [YKA]), and the Siberian sector (Kislovodsk [KIV], Norilsk [NRIS], Peleduy [PDY], Tiksi [TIXI], Yakutsk [YAK], and Zalesovo [ZAL]). Two stations from each geographical sector will be exemplarily used in the figures. Particularly, station KIV located at only 42° E and 43°N was only used because the availability of data for some of the decisive events from stations farther east is scarce. Thus, we have relatively huge azimuthal gaps for waveform analysis and did not try a reanalysis of moment tensor solutions.

3 Methods and results

3.1 HYPOSAT locations of the swarm events

After intercomparison with several other location tools such as HYPO71 (Lee and Lahr 1975), HYPOCENTER (Lienert and Havskov 1995), and ISCloc (Luckett and Storchak 2001), we used HYPOSAT (Schweitzer 2001) as one of the advanced classical global location tools for relocation of the swarm:

- It is classical in the way it uses the Geiger method for locating earthquakes.
- It allows the selection of confidence levels for error ellipses that we chose as 95%, the error is handled as rms values as well as distance errors in all spatial directions.
- It documents the search for location solutions far away from solutions already found in previous iterations and thus documents the robustness of the hypocenter solution (better than HYPOCENTER).
- It uses an arbitrary regional velocity model and can also use a global velocity model in farther distances from the source location (better than ISCloc). In our case, we used the IASPEI-91-model (IASP91; Kennett and Engdahl 1991; Kennett et al. 1995) or the preliminary reference earth model (PREM; Dziewonski and Anderson 1981) which has been shown to work better in marine environments (Reves-Sohn, personal communication) as the global model. We varied the regional models according to Fig. 3 later in the processing.
- It can process all the information available in the ISC dataset, i.e., slowness values, amplitudes, and arrival times (better than HYPO71 or HYPOELLIPSE).

The original dataset from ISC was mainly weighted according to distance to the source and

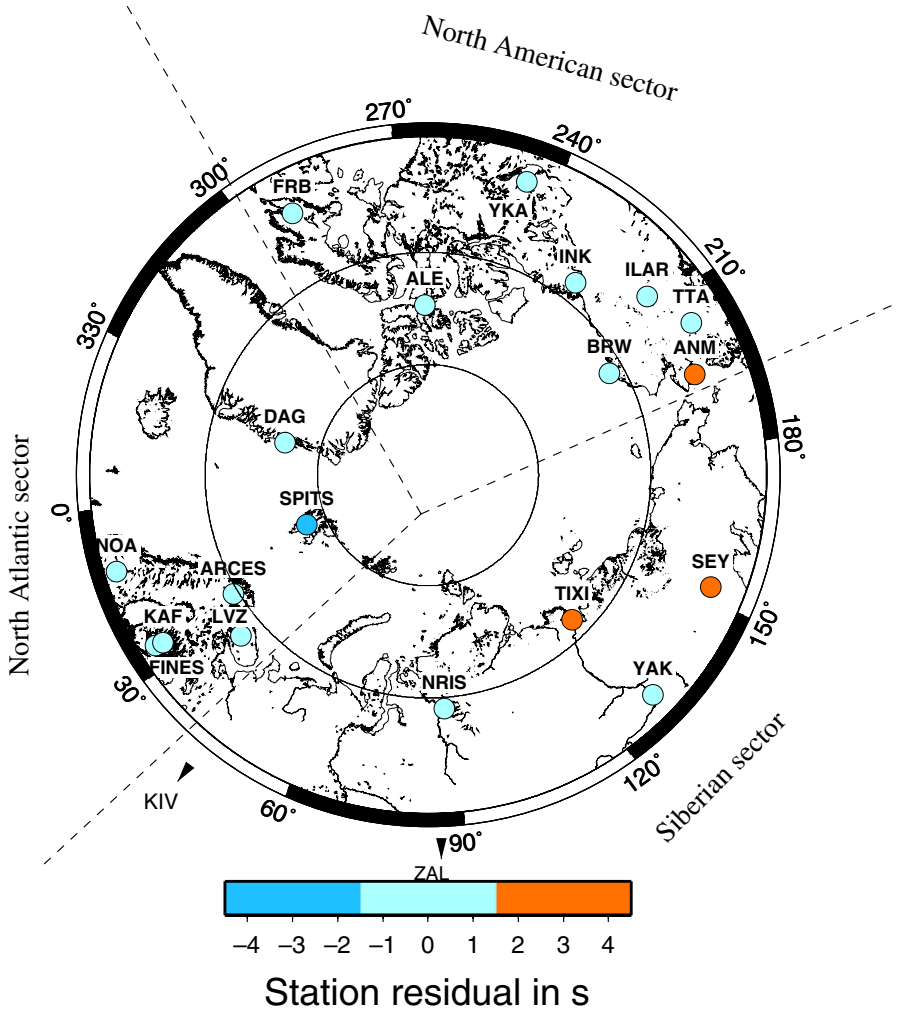

Fig. 2 Average station residuals constructed from histograms as in Fig. 6 for the entire Arctic region north of 60° N. Each *circular line* is a 10° latitude separation and the label surrounding the map indicates longitudes. Three sectors are discussed in the text and the following figures, which are separated by *dashed lines* that meet where the swarm activity is centered. Two stations of each sector will be exemplarily displayed (SPITS and DAG for the North Atlantic sector, KIV, situated outside the map—see text—and TIXI for the Siberian sector and INK and YKA for the North American sector, thus KBS, which is very similar to SPITS, and ZAL, which does not show sufficient data, were not displayed). Note the marked divergence of station residuals from 0 s in Spitsbergen and Eastern Siberia/Alaska. All stations used for waveform correlation are shown except KBS which is located too close to SPITS array

travel time residual, although heterogeneities in the subsurface can disturb such a trivial setup and the regional velocity model is unknown. Velocity models from nearby locations investigated by Jokat and Schmidt-Aursch (2007) deviate strongly from IASP91 and PREM. To unfold the effects of location algorithm, weighting, local heterogeneities, and regional velocity model, we relocated the events using the IASP-91 model and no phase weighting in HYPOSAT with a starting depth of 10 km. Schweitzer (2006) describes a similar procedure to improve ISC locations. The rms error of the original swarm data in HYPOSAT we obtained was ~1.46 s (HYPOSAT baseline quality). Naturally, our aim was not only to achieve better than this relatively high values but to achieve better values than the original ISCloc dataset of ~1.14 s, which naturally delivers a

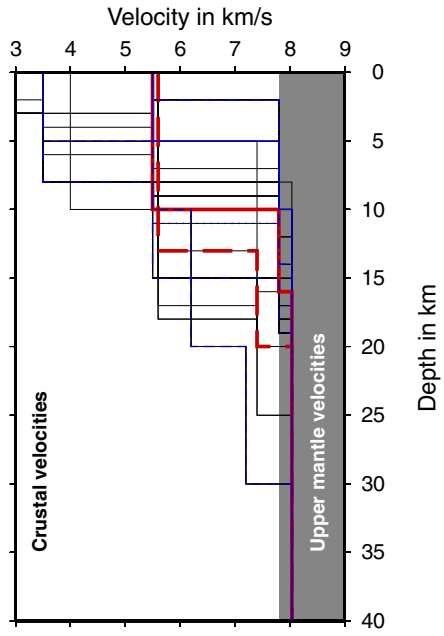

Fig. 3 Compressional velocity (vp) over depth plots which have been used in the hypocenter inversion to optimize the regional vp model are displayed. Where vp assesses an upper mantle value of 7.8 km/s or higher, the area of the plot is underlain by *gray*. In *blue*, five arbitrarily chosen models with various textures are shown that have been used for creating the OLD dataset described in the text. The models in *red* exhibit the lowest rms time residuals and are interpreted as the optimum velocity models. They adopt mantle velocities at 16 or 20 km depth, respectively. The *continuous red line* shows the slightly better model with a Moho at 16 km, which has been used in further elaborations in the text

better value since only P arrivals are evaluated for location.

In the following, we tried to optimize the regional velocity model. Seismic events usually occur in the solid earth. In the teleseismic case, they are mostly registered on land. Thus, although the survey area around the Gakkel Ridge is entirely submarine with an average of around 4,000 m water depth, inserting a water layer into our velocity models would be erroneous because it implies that a water layer is modeled both at source and receiver location. Thus, the shallowest part of the velocity model should be an average image of the subseafloor structures.

We used classical P velocities for MOR environments (Kearey and Vine 1990) and local seismic velocities deduced from unreversed refraction profiles by Jokat and Schmidt-Aursch (2007) which showed an upper crustal velocity of around 5.6 km/s and a lower crustal velocity of 7.4 km/s in a similar geologic setting further west at Gakkel Ridge. We varied the depth of the classical layers of the MOR and the Gakkel Ridge layers and came up with a set of 124 different velocity models (62 different regional models, see Fig. 3, multiplied by two global models). Five velocity models from this set with and without sediment layers (i.e., velocities below 4 km/s) and with crustal thicknesses varying from 2 to 30 km (blue in Fig. 3) were used to create an offset-limited input dataset (OLD) from the whole ISC bulletin readings.

The near-offset arrivals appear more sensitive to variations of the regional velocity model and are best used to optimize the regional velocity model. We checked the nearest arrivals of our event database up to a distance of 30° for robust solution in location. Any event that delivered extremely large rms errors and/or could not find a better hypocenter solution in comparison to the HYPOSAT baseline quality and/or was not robust in space (i.e., located at a completely different spot when varying the velocity model) was deleted from the test dataset, so that only 87 events made up the OLD to optimize our velocity model.

So, we tested all 124 regional P velocity models for those 87 OLD events. The velocity model in depths higher than those shown in Fig. 3 was filled by either of the two global models mentioned above (IASP91 and PREM). Also, arrivals further away than the maximum range of validity of the regional model (variable *maxdis* in HYPOSAT, see Schweitzer 2001) were only modeled by IASP91 or PREM.

On top of varying the velocity model, we varied *maxdis* from 5° to 30° and the starting location depth from 5 to 50 km. All tested parameters change the location solution in a nonlinear manner. However, there is a trend that a *maxdis* of 20° and a starting location depth of 10 km generally deliver the best results.

The best models from our selection provide a best average rms time residual of ∼0.90 s for the OLD and correspond to a sediment-stripped oceanic-type crust of 16 to 20 km thickness (both red in Fig. 3). We will restrict our further analysis

to the slightly better model with 16 km crustal thickness. When using the complete dataset with this optimized velocity model, we decrease the rms error increases to ∼1.23 s, which is still 0.09 s higher than the ISCloc value, but 0.23 s better than the HYPOSAT baseline quality. We could not cross-check our model with gravity data because the nearest detailed surveys were conducted at 60° E or 95° E (Coakley and Cochran 1998), respectively.

In the original records, the epicenter locations cluster around 85°37′ N and 84°40′ E and the swarm is elongated along the rift axis of Gakkel Ridge. The focus of seismicity in the complete relocated set of data is situated at 85°35′ N and 85° E, i.e., slightly southwest of the original records and thus shifting the swarm location from the northern flank to the rift valley slightly north of the southern flank of Gakkel Ridge (most relocations in Fig. 4 show some easterly component), the elongation remains similar. The lateral error is uniformly distributed for the best events with a circular error ellipse of around 2–3 km radius for 95% confidence; for the other events, an elongation of the error ellipse along the rift valley is observed with azimuths of 110° to 150° (Fig. 5). Most events with a high number of reported phases in the ISC catalog (>50 phases) plot in the central valley of Gakkel Ridge in a narrow longitude band of ±1° along 86° E (Fig. 5).

The semimajor axis of the overall error ellipse in Tolstoy et al. (2001) is equal to the HYPOSAT baseline quality of 16 km. By using our best model, we relocate the earthquakes as accurately as possible, but a semimajor axis of the overall error ellipse of 10 km remains. This uncertainty is

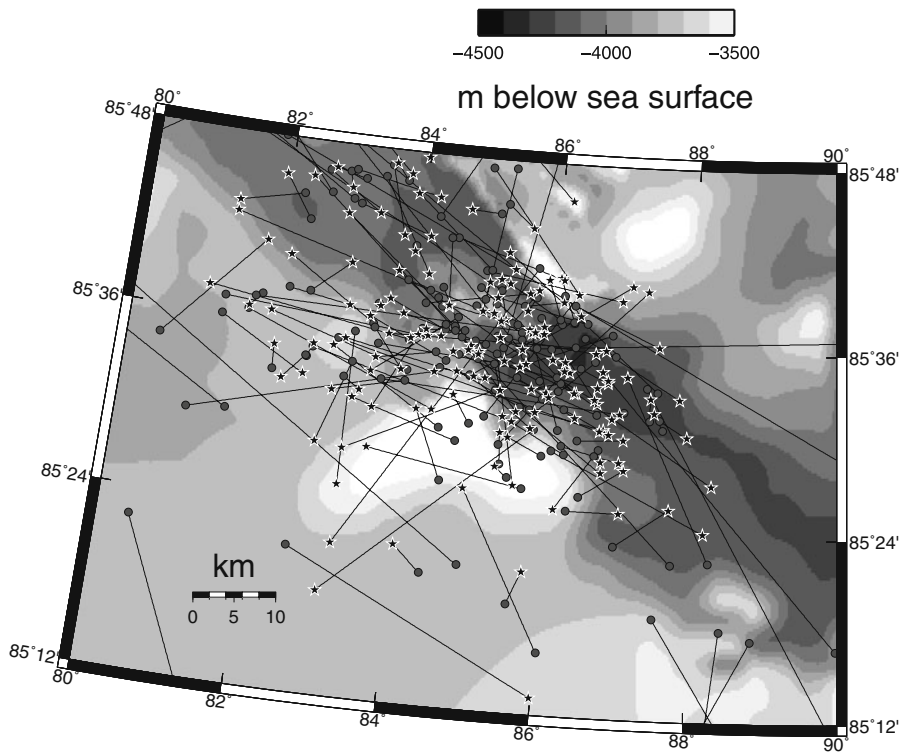

Fig. 4 The epicenters of the seismic events of the swarm are plotted on top of the bathymetry. Original positions of the ISC location are marked by *dark gray circles* as in Fig. 1, whereas new HYPOSAT locations are marked by *black stars* as in the following figures. Here, they have been *outlined in white* to help the eyes of the reader to distinguish between the two locations. The same events are linked by *black lines* to display the movement during the relocation. No obvious trend is observed; however, most events are somehow moved to the east. The distribution of epicenters before and after relocation is similar and roughly spans an area of 60 × 30 km along the rift valley

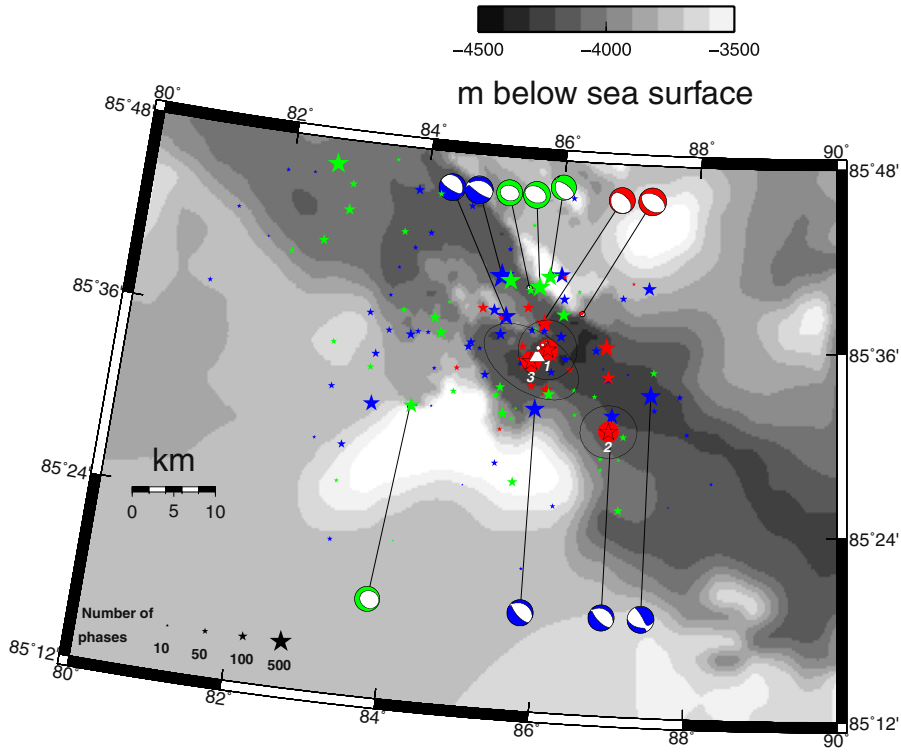

Fig. 5 The epicenters of the HYPOSAT location are plotted as *colored stars* on top of the bathymetry. For the three numbered events (*stars underlain by circles of the same size* mark these events with similar waveforms listed in Table 2), error ellipses have been drawn (*circles* with ∼3 km radius for events 1 and 2 and an *ellipse* with semimajor axis of 9.5 km for event 3). The high-magnitude events which provide moment tensor solution are shown by upper hemisphere projections of the moment tensor. All event epicenters and moment tensor solutions are marked in colors according to their phase of occurrence (*blue* initial phase A, *red* potential vent opening phase B, *green* late phase C) discussed in the text. The close location in space of a *blue* moment tensor and one of event 2 is random and bears no significance for the rupture process encountered in event 2. The size of the event stars displays the number of phases used in the final HYPOSAT location. All events marked in *red* and nearly all events with more than 100 phases used in the final inversion are located in the central rift valley. A *small white triangle* (volcano) close to events 1 and 3 marks the position of the crater of Oden volcano which was discovered by Sohn et al. (2008)

unavoidable as the nearest stations to the earthquake swarm are 1,000 km away. Our geological interpretation bears this location accuracy in mind.

The hypocentral depth of the majority, i.e., 71 of 87 (81%), events lies between 10 and 60 km using the best velocity model and the OLD (Fig. 6). Using the complete dataset, the maximum depth of the majority of events decreases to 45 km (187 of 237 events, i.e., 78%). The average depth error is 32.4 km at a confidence level of 95%; however, for the OLD, it is only 20 km; for intracrustal events, it decreases to 10 km; and for events with more than 30 registered phases (115 out of 237), it drops to 5.5 km. Most events in both cases are situated slightly below the seismic Moho at 16 km depth or close to the surface. Even some of the OLD events in the upper mantle exhibit depth errors smaller than 30 km and cannot be located within the crust. Using a starting location at 20 km depth produced worse results than at 10 km, indicating that the inversion has a tendency to increase the depth of events, a smearing along the raypath that is observed in all kinds of nonlinear seismic inversion processes such as local earthquake tomography. We are unable to quantify the extents of smearing, but the documented errors of HYPOSAT indicate they are not of the order

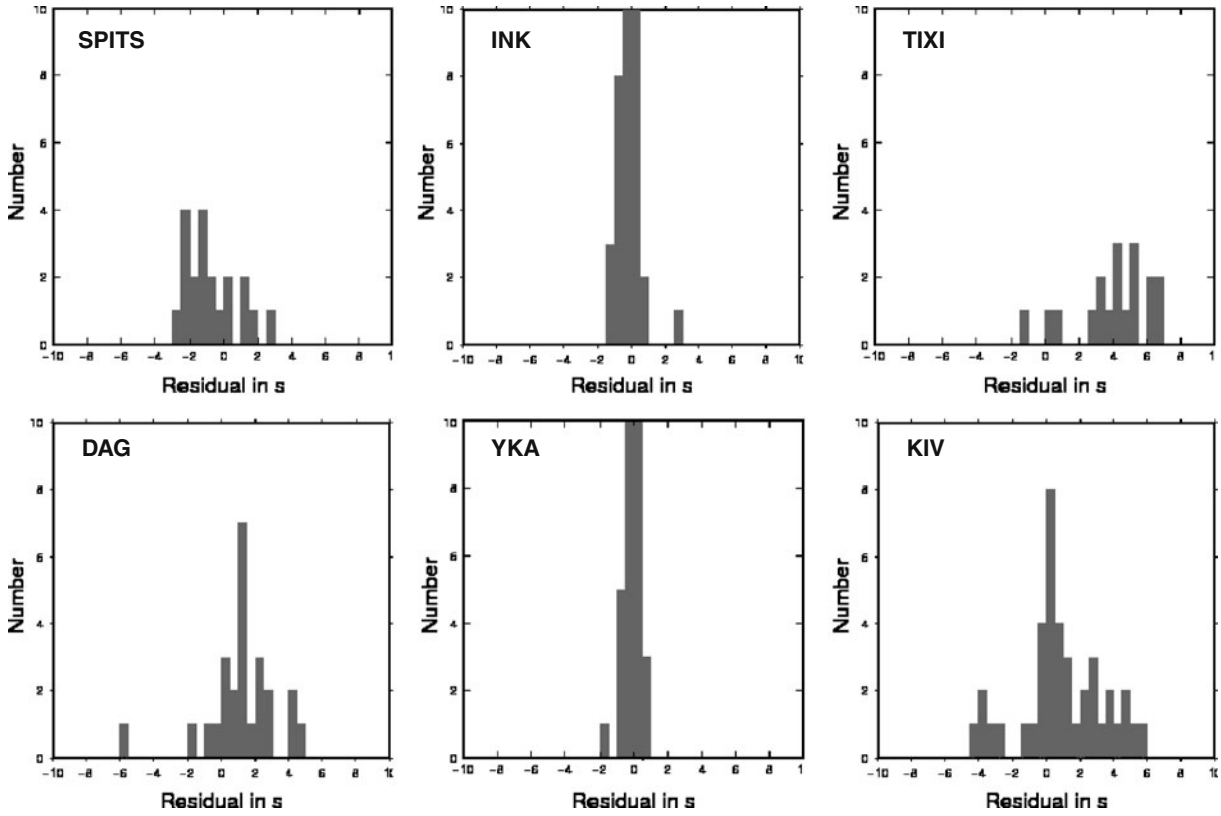

Fig. 6 Histograms of event time residuals within the six stations plotted in and mentioned in the caption of Fig. 2, i.e., SPITS and DAG for the North Atlantic sector, INK and YKA for the North American sector, and KIV and TIXI for the Siberian sector. Trivially, SPITS and TIXI phases are more rarely used in the final location of HYPOSAT because of the high time residuals, which explains the lower number of events in the histograms

to lift the events from the upper mantle into the crust.

3.2 Station residuals

In the following, we studied the travel time residual analysis of single stations. We estimated the typical station residual by plotting a histogram for all events located in a band of 1° latitude surrounding the focus of seismicity only allowing events with rms residual better than 1 s and a depth smaller than 45 km and binned the values into 0.5 s residual stripes (for examples, see Fig. 6). Most frequently, we obtain a unimodal distribution and searched for the peak.

Peaks, generally, scatter around 0 s residual (light blue color on Fig. 2). However, there is a trend toward big delays (>2 s) in eastern Siberia (stations TIXI and SEY) and westernmost Alaska (station ANM) and strong negative values in Spitsbergen (stations KBS/SPITS). This trend is so strong in the direction of the northernmost Atlantic that the Spitsbergen stations KBS and SPITS usually are not considered in the final solution of HYPOSAT (the number of residuals considered for the analysis of residuals at SPITS is only five of 20 plotted in Fig. 6). There have been reports about time shifts in Spitsbergen stations (Gibbons 2006), however, they did not occur during the observation period and, thus, bear no relevance to our observation. Only two arrivals were picked for Jan Mayen island and no arrival at all was documented in Iceland (Vogfjord, personal communication). The heterogeneity of structures in the Barents Sea (Ritzmann et al. 2007) might play a minor role in producing this delay. The shal-

low structures in the Barents Sea are not sampled directly by seismic rays arriving at Spitsbergen, but could interfere for some events.

Last but not the least, we observe that the phases notoriously arrive earlier in the northern North Atlantic direction than predicted by theoretical models. Hence, they must propagate faster and traverse a large area of higher seismic velocities than incorporated in the regional velocity model. The opposite is true for the stations in westernmost Alaska.

3.3 Cross-correlation analysis

We reassessed the quality of the location dataset by inspecting the waveforms of the nearest stations with publicly available waveforms. This procedure helped to exclude picking errors by the reporting agencies, which we eradicated from the set of data, and allowed us to find spatially clustered events with coherent waveforms. We calculated the coherency value as in Maurer and Deichmann (1995): similar waveforms are grouped by calculating the coherency value as ratio between cross-correlation and the square root of the autocorrelations of the single events.

In our case, we used a time window of 16 s around the first arrival (mostly the normal P wave) to include the decisive parts of the single waveforms in our analysis. The correlation window was shifted sample by sample up to a maximum of 8 s in both directions to calculate the maximum coherency in all three components as described in Hensch et al. (2008) and this value was thresholded at a value of 0.6 to 0.7 to group similar waveforms depending on the station. Events with a coherency higher than the threshold are considered as similar. During this initial correlation step, many well-correlated events were detected for single-station datasets. An example of the results

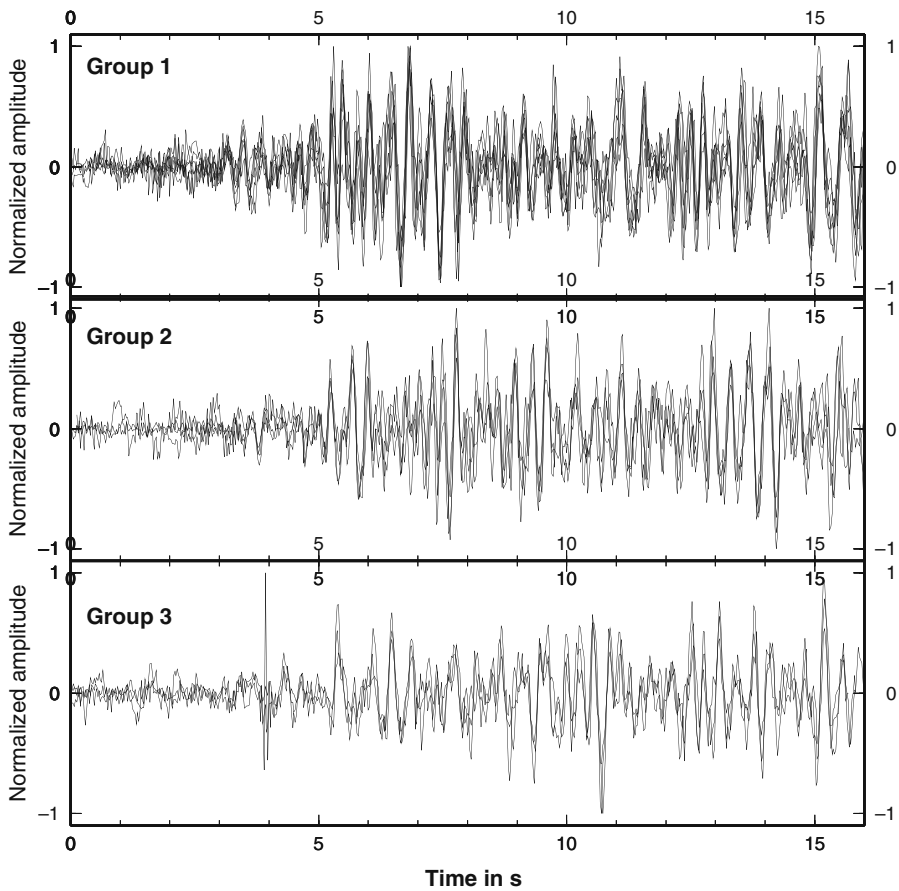

Fig. 7 Three groups of similar events were found for the station SPB4 of the Spitsbergen array SPITS during the station-wise cross-correlation procedure described in the text. The waveforms of the vertical component are plotted in 16 s time windows normalized to the highest amplitude

Table 1 Stations used in the waveform analysis in this study with sample rate of downloaded data and bandpass filter limits used for processing

Station (array if applicable)	Sample rate (Hz)	Filter lower limit (Hz)	Filter upper limit (Hz)
SPB4 (SPITS)	40	1	20
INK	40	1	20
PDY	40	1	20
NRIS	40	1	15
ARC2 (ARCES)	40	1	15
YKW3 (YKA)	100	1	10
YAK	40	1	10
LVZ	20	1	10
DAG	20	1	10
IL31 (ILAR)	20	1	10
KIV	40	1	8
TIXI	40	1	5
ZAL	40	1	5
ULM	40	1	5

The stations are sorted according to the filter width, which depends on sample rate, distance to the earthquake source, and quality of the data

is given for station SPB4 of the SPITS array in Fig. 7, which shows good correlation even at high frequencies due to the relative proximity to the source area. Sample rates of the data used for the various stations are shown in Table 1.

Within each group, a master event was defined as the event with the least rms residual in the relocated OLD dataset and its delay was set to zero. The arrivals of other events were shifted accordingly by using the delay calculated from the shift of the time series toward each coherency maximum. We relocated the entire dataset using the improved phases but obtained no significantly different results as the percentage of corrected phases of coherent events in the total dataset is small.

If similar events can be detected on more than one station, Maurer and Deichmann (1995) propose that the source process of such events has to be almost identical. Two earthquakes only produce similar waveforms at two seismic receivers if the distance between the earthquakes does not exceed a quarter of the dominating seismic wavelength and the source process is the same. A simple binary logical test was performed to find matching pairs of events. Two events were considered similar if they produced at least at two stations coherent waveforms. Only three of the 237 events (see Tables 2 and 3) are so similar that we actually find matching patterns (Fig. 8). All of them occur between 5 and 9 April 1999 and HYPOSAT places them in the central rift valley of Gakkel Ridge with events 1 and 3 being located extremely close to Oden volcano (Sohn et al. 2008) and to each other (see Fig. 5). The significance of the time shifts introduced by the cross-correlation can be explored in the following chapter about double-difference location where raw and corrected values of interevent times are explored (see Table 3).

We further analyzed the first motion of the P phases of events 1 to 3 in our set of equiazimuthally distributed waveform records. All three events yield a compressive first motion on all analyzed vertical components with the exception of the station INK where it is unclear whether the positive first motion can be confirmed. This strongly indicates a deviation from the classical P wave radiation pattern of a double-couple source and indicates a volumetric expansion component in the source mechanism of these events.

3.4 Double-difference location

The double-difference algorithm of Waldhauser and Ellsworth (2000) has been widely used to calculate relative locations of earthquakes in a

Table 2 The locations of the three clustered events with similar waveforms (see Fig. 8) marked in Fig. 5 with the final origin time as date and time in GMT, HYPOSAT location in latitude, longitude, and depth, the corresponding axes of the error ellipses, and finally, their body wave magnitude

Event	Date	Time	Latitude (° N)	Longitude (° E)	Error latitude (km)	Error longitude	Depth	Error depth (km)	Magnitude m_b
1	05/04/99	08:08:36	85.59	85.92	3	3	12.6	1.4	4.5
2	06/04/99	10:05:24	85.51	86.84	3	3	14.6	1.2	4.4
3	09/04/99	01:05:58	85.52	85.4	4	6	16.4	1.6	4.5

Table 3 Arrival times in day (DD), hour (HH), minute (MIN), and seconds (SEC) and travel time difference with respect to the arrival of the P wave at SPITS are displayed for events 1–3 for those stations in a maximum distance of 3,600 km distance from the source (Offset) which registered all three events and for KIV out of consistency reasons laid out in the text

Station	Azimuth	Offset	Event 1				Event 2				Event 3				Travel time difference to SPITS (s)			RDD (s)			
		(km)	Arrival time				Arrival time				Arrival time							dt_{RDD} (1, 2)		dt_{RDD} (1, 3)	
			DD	HH	MIN	SEC	DD	HH	MIN	SEC	DD	HH	MIN	SEC	t_1^*	t_2^*	t_3^*	Raw	Corrected	Raw	Corrected
SPITS	*262*	1,240	5	8	11	11.5	6	10	8	3	9	1	8	36.3	0	0	0	0	0	0	0
DAG	*300*	1,679	5	8	12	8.3	6	10	8	57.4	9	1	9	31.2	56.8	54.4	54.9	−2.4	−0.05	−1.9	−1.75
TIXI	*125*	1,717	5	8	12	17.1	6	10	9	6	9	1	9	40.1	65.6	63	63.8	−2.6	0	−1.8	−1.8
ARCES	250	2,089	5	8	12	55.1	6	10	9	45.3	9	1	10	17.9	103.6	102.3	101.6	−1.3	−0.07	−2	0.63
YAK	129	2,786	5	8	14	0	6	10	10	49.4	9	1	11	24	168.5	166.4	167.7	−2.1	0.35	−0.8	−0.8
INK	*32*	2,828	5	8	14	4.1	6	10	10	53.7	9	1	11	27.4	172.6	170.7	171.1	−1.9	0	−1.5	−1.5
SEY	104	2,858	5	8	14	9.5	6	10	10	59	9	1	11	34	178	176	177.7	−2	0.35	−0.3	−0.3
FINES	246	2,973	5	8	14	16.3	6	10	11	5.5	9	1	11	38.7	184.8	182.5	182.4	−2.3	0.05	−2.4	−2.4
ILAR	45	3,145	5	8	14	31.1	6	10	11	20.6	9	1	11	53.7	199.6	197.6	197.4	−2	−0.85	−2.2	−1.65
YKA	*17*	3,548	5	8	15	1.6	6	10	11	50.7	9	1	12	24.5	230.1	227.7	228.2	−2.4	−0.05	−1.9	−0.07
KIV	*226*	4,788	5	8	16	38.4	6	10	13	27.6	9	1	14	1.6	326.9	324.6	325.3	−2.3	0.05	−1.6	−1.52

From these values, referenced double-difference times (i.e., interevent differences) have been calculated (raw) and corrected by delay times calculated from cross-correlation (corrected) between events 1 and 2 and events 1 and 3. The stations closely analyzed in the figures have been printed in italics

limited source area greatly improving the location quality. This, however, requires many well-connected coherent events with similar waveforms on several stations. Since only three of our events fulfill the similarity criterion, a relocation of the entire swarm with this method did not promise considerable improvement of the location quality. We still analyze relative travel times of the three coherent events to assess their relative location.

The double difference as defined by Waldhauser and Ellsworth (2000) using travel time for the first event t_1 and travel time for the second event t_2 is:

$$\mathrm{dt_{DD}} = t_1 - t_2.$$

We can also express this in terms of an approximately constant time arrival t_{S_0} at a close station S_0 as:

$$t_1^* = t_1 - t_{S_0,1} \quad \text{and}$$

$$t_2^* = t_2 - t_{S_0,2}\,.$$

Assuming the events are close in space and, thus, travel time differences to the reference station are equal, we can calculate a referenced double-difference time with respect to S_0:

$$\mathrm{dt_{RDD}}\,(1,2) = t_1^* - t_2^* = \left(t_1 - t_{S_0,1}\right) - \left(t_2 - t_{S_0,2}\right)$$

which we calculated in Table 3. If $t_{S_0,1}$ equals $t_{S_0,2}$, then the referenced double difference (RDD) will equal the real double difference. So, in Table 3, we show the referenced $\mathrm{dt_{RDD}}$ for "raw" travel time values from the bulletin and for "corrected" travel times including delay times calculated from the cross-correlation. Only stations with arrivals from all three events and within 3,600 km from the source were used, with the exception of KIV that was used because of the scarcity of data in the Siberian sector (see above).

The RDD with respect to SPITS between events 1 and 2 is nearly 0 s for all the stations listed. Locating only by these stations should provide us with the same location for the two events. This not being the case shows that the emphasis during the location procedure is not on the few stations situated in close proximity to the source.

Between events 1 and 3, which are located very close in space to each other using HYPOSAT, an

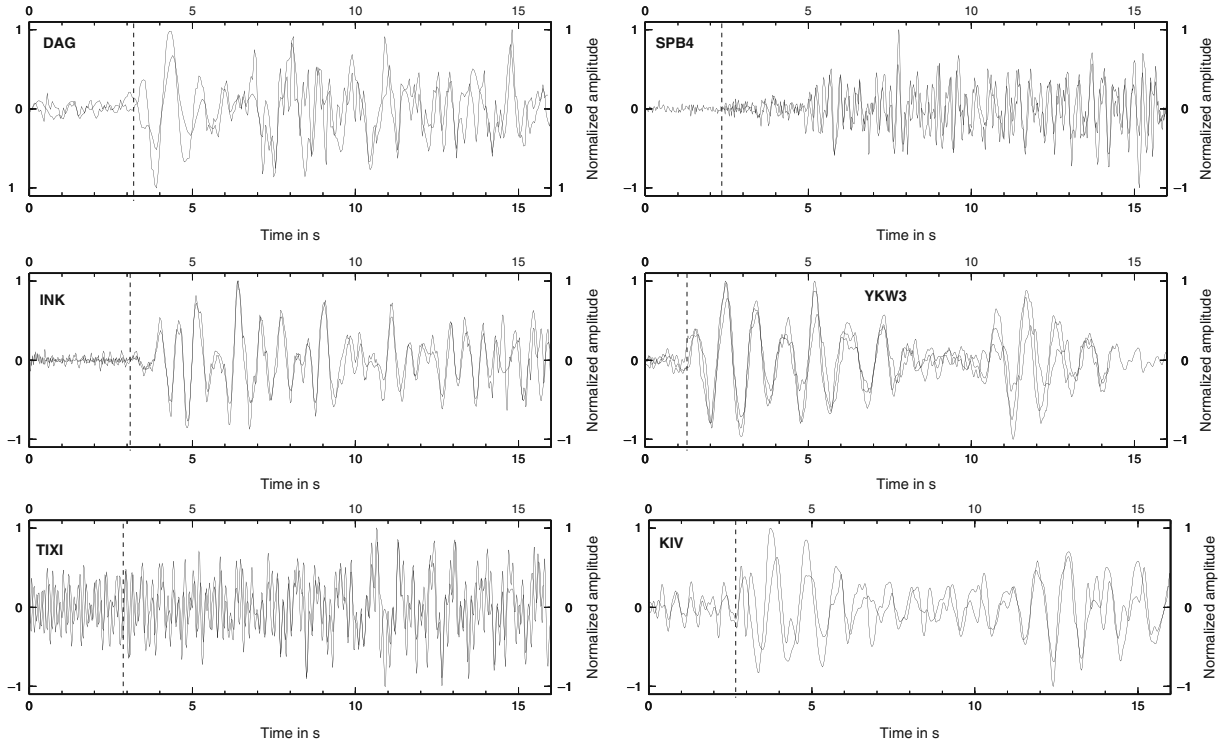

Fig. 8 When correlating waveforms at different stations, only three similar events can be detected. The vertical component of the event waveforms for the six stations also used in Fig. 6 are displayed in the figure in 16 s time windows normalized to the maximum amplitude. The picked first arrival has been marked by a *vertical dashed line* to show the positive amplitude of most first arrivals. For SPB4, the three events are part of group 2 in Fig. 7. YKW3 is part of the Yellowknife array (YKA) and data with 100 Hz sample rate could be used for this station

average dt_{RDD} of ~1 s remains. So, the overall HYPOSAT location was actually produced by phases further away from the source. On top, there is neither an obvious relation between distance to the source and dt_{RDD} nor between azimuth and dt_{RDD}, so the average dt_{RDD} of 1 s reflects the minimum error of location. Since the rays travel mostly within the upper mantle, this is equivalent to around 8 km lateral error. The lateral error of HYPOSAT at 95% confidence level is thus an underestimation of around 25%.

All three events as laid out must reflect the same process to assume similar waveforms, all events are located between 12.6 to 16.4 km depth, all of them are located in the central rift valley, events 1 and 2 are indistinguishable up to 3,600 km offset from the source and events 1 and 3 plot nearly on the same spot close to Oden volcano (Sohn et al. 2008). Thus, either this volcano or another vent aligned with Oden's chain of volcanoes and located further to the SE is the most probable source region for the repetitive events.

3.5 Magnitudes

The occurrence of high magnitudes is the most unusual feature about the earthquake swarm and is the basic reason why it was detected worldwide. Typical oceanic earthquake swarms at volcanic ridge areas normally reach their highest magnitude somewhere around a maximum magnitude of 5 or higher (Fox and Dziak 1998; Dziak et al. 2004); however, the amount of such earthquakes is unique at Gakkel Ridge. Making a crude but empirically supported estimate (Utsu 2002)

by equating body wave magnitude with moment magnitude scale following Kanamori (1977):

$$M_0 = 10^{1.5\,\mathrm{mb}+16.1},$$

estimating a typical stress drop Δsigma of 1,000 bar for the average magnitude 4 earthquake and assuming a small earthquake with a circular fault shape (Ruff 2002), i.e.:

$$\Delta\mathrm{sigma} = (7/16)\, M_0/r^3,$$

we expect a median fault radius of 176 m for each of the events. Just using the well-located OLD events, a total of 30 km of crust in vertical and/or horizontal direction could be cracked by the events if they imaged, for example, a tectonic process or propagation of fluid-filled cracks (Dahm 2000). For such a process to occur, seismicity should cluster densely, marking one fault plane or the tip of the propagating dike. Instead, we observe that, even after relocation, seismicity remains distributed over a large area of 60 × 30 km throughout the swarm (Fig. 5), discouraging a single dyke ascent as the driving force. However, a pure tectonic origin of the swarm is also unlikely. It should produce aftershock sequences with decaying magnitudes which is not observed. High-magnitude events (with body wave magnitude $m_b > 5$; National Earthquake Information Center [NEIC]) occur throughout the entire swarm period (Table 4); however only 1 day, 1 February 1999 (14 days after the beginning of the swarm) is marked by three such events and shows that a large amount of energy is released in the initial phase of the swarm. The first and the third event on this day show four aftershocks, i.e., further teleseismically registered events within a radius of 10 km with decaying magnitudes. This tectonic process is overprinted by additional seismicity scattered in the area. The largest event occurs at the end of March shortly before the three similar events mentioned above. The large-magnitude events in April and later are single events without any related low-magnitude seismicity in time and space. Most of these late high-magnitude events are centered slightly north of the focus of seismicity on the northern rift flank.

Except for one event (26 May 1999), all large events have a moment tensor solution. We show the calculated percentage of double-couple component following Jost and Herrmann (1989) in Table 4. There is a first low value in mid-March 1999 and a dramatic permanent decrease to values around 80% and lower at the end of April 1999, i.e., shortly after the occurrence of the three similar events mentioned above.

Table 4 All events with higher body wave magnitude than 5, their hypocentral depth for the best location solution, and the percentage of the double-couple component in the moment tensor solution from one of three sources (NEIC: National Earthquake Information Center/USGS, Harvard: Harvard centroid moment tensor solution, GCMT: http://www.globalcmt.org)

Event date	m_b (NEIC)	Calculated depth	Percent double couple	Reporting agency
1999/02/01 04:52	5.1	14.6	96	Harvard
1999/02/01 09:56	5.1	15.1	93	Harvard
1999/02/01 11:56	5.1	14.9	88	NEIC
1999/02/19 19:10	5.1	18.5	98	GCMT
1999/02/22 08:02	5.2	15.6	94	Harvard
1999/03/13 01:26	5.3	16.5	85	Harvard
1999/03/21 15:24	5.4	15.5	53	GCMT
1999/04/01 10:47	5.1	15.2	98	Harvard
1999/04/26 13:20	5.2	15.0	76	Harvard
1999/05/18 20:20	5.1	15.9	85	Harvard
1999/05/26 23:56	5.1	20.6	Not calculated	
1999/06/11 23:54	5.1	Not calculated	38	Harvard
1999/06/18 19:49	5.3	16.1	51	Harvard

Only 11 of the 13 moment tensors are located in the region displayed in Fig. 5

3.6 Spatiotemporal organization of the swarm

Figures 5 and 9 show the evolution of the swarm in space and time. To be independent of single outliers in focal depth and, thus, to get a representative view of depth of hypocenters over time, we calculated the median depth of five subsequent events for the entire swarm by shifting the averaging window by three events such that an overlap of two events exists for all neighboring groups. These results are also plotted in Fig. 9.

The swarm sequence starts at shallow depth. Hypocenters range across the entire crust and upper mantle in ascending and descending phases before focusing in the lower part of the crust and the uppermost part of the mantle between 10 and 20 km at day 40 and, finally, the crust–mantle boundary at day 60. In this initial phase (phase A, blue in Figs. 5 and 9) of the swarm, five out of 13 seismic events with magnitude above 5 occur. These events are predominantly normal faulting earthquakes following rift valley bounding faults at the base of the crust in 14 to 19 km depth (accepting a dip of 60°, the events would situate 8 to 10 km inside from the morphologically high rift walls—all events fulfill this criterion) with high percentage of double-couple mechanism. Laterally, the hypocenters are distributed in a 60 × 30-km long band around the median valley and show the highest depth variation, which indicates brittle behavior of the entire lithosphere/crust typical for tectonic events.

After day 70, seismicity enters a second phase (phase B). Hypocenters now follow a migration path of decreasing depth in the crust (bars marked in red and events surrounding it on Fig. 9) from the crust–mantle boundary to values below 10 km until about day 100. Apart from the odd events occurring further west, seismicity in phase B concentrates in the rift valley close to the crater of Oden volcano (Sohn et al. 2008) and around the three events with very similar waveforms (encircled stars in Fig. 5) which occur at the end of this phase.

Subsequently, hypocenters can range down to 30 km before they essentially focus in a 5-km thick region above the crust–mantle boundary (Fig. 9). During the entire phase, the epicen-

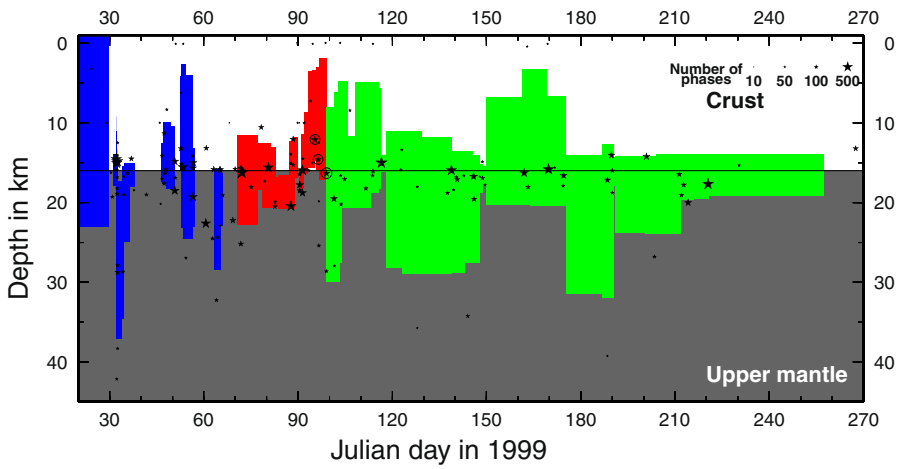

Fig. 9 Hypocenter depth of the events in the study area is plotted over time displayed as Julian days in the complete year 1999. No events were registered after Julian day 267, 24 September. The single hypocenter depths are marked as *black stars*, which are sized according to the number of phases used in the final hypocenter inversion (see scale in *upper right corner*). *Colored horizontal bars* represent the median and 80% confidence level of a group of five follow-up events and the time range the group is spanning. In time periods when the 80% confidence level spans the entire depth range, no horizontal bar is drawn. An overlap of two events occurs from one bar to the next. The bars are painted in colors according to their phase of occurrence as in Fig. 7a (*blue* initial phase A, *red* and *gray* potential vent opening phase B, *green* late phase C). The seismic Moho is marked by a *line* and the upper mantle is shaded in *gray* to visualize hypocenter depth in comparison to the underlying velocity model. The three events with similar waveforms are *encircled*

ters scatter again in a larger area (Fig. 5), but the best located events occur in the uppermost mantle from 16 to 20 km depth. High-magnitude events in phase C expose the highest percentage of nondouble-couple components. Without the nondouble-couple component disappearing from the high-magnitude event, seismicity suddenly ceases with an intracrustal event on 24 September 1999 (Julian day 267) marking the end of the swarm (Fig. 9).

4 Interpretation and discussion

The seismic swarm forms a NW–SE-oriented elongated hypocenter cluster extending a minimum of 60 km along the rift valley of eastern Gakkel Ridge. The focus of activity is at 85°35′ N and 85° E where a prominent chain of volcanic cones including Oden volcano was detected by Sohn et al. (2008). Seismicity concentrates at this central volcanic ridge in the rift valley, the bounding rift valley faults to the north and south and extends over the southern rift flank. The swarm is untypical for a purely tectonic event sequence. The earthquake magnitudes mostly do not follow an Omori law because typical aftershock sequences are the exception and seismic energy release occurs in a wide range of magnitudes not only related to previous earthquakes in the series. The widely scattered lateral distribution of events even after relocation supports a seismic activation of a large area rather than a failure of distinct faults. Concentration around a narrow area occurs after 70 days, when also a constant decrease of hypocentral depth is observed. This is typical for fluid-driven seismicity. Late high-magnitude events showing nondouble-couple moment tensors support such a scenario.

On the other hand, the swarm differs from typical MOR dike intrusion events as it contains high-magnitude earthquakes and shows an unusually long duration of 8 months rather than a few weeks. Tolstoy et al. (2001) analyzed the original ISC locations and grouped large portions of events over time so that they found a lateral migration of seismicity over time. A migration of seismicity over time would be typical for fissure eruptions as, e.g., in the classical case study at Krafla in Iceland (Einarsson and Brandsdóttir 1980). Instead, after a detailed analysis of the error of location, seismicity remains scattered over a large area throughout most of the swarm (Fig. 5).

We, therefore, propose a different interpretation of the swarm dividing it into three phases with different characteristics:

4.1 Phase A

We believe that the initial phase of the swarm represents a tectonic activation of the ridge segment. This phase includes five of the high-magnitude events ($m_b > 5$) of the swarm. It activates the entire crust and upper mantle in the early part, focusing to lower crustal levels after day 40. Tectonic seismicity from brittle failure is typical for upper crustal and mid-crustal material. Occasional shock–aftershock sequences and predominant double-couple source mechanisms support this idea. Not well-correlating waveforms of the seismic events throughout this phase indicate that the crustal structure is very heterogeneous and that events occur in a large subsurface volume. The spatially wide distribution of epicenters from HYPOSAT ($60 \times 30 \times 45$ km) or even the original ISCloc results are reasonable images of the distribution of seismicity (blue on Figs. 5 and 9).

4.2 Phase B

After day 60, the b value increases (Müller and Jokat 2000), indicating an increasing proportion of smaller events and less large events, thus imaging the decrease to lower effective stress in the subsurface. Since fluids in magma chambers (Daines 2000) and the increase of pore pressure through interaction of magma with groundwater (Wiemer and McNutt 1997) pose as buffers for effective stress, high b values are frequently produced by volcanic seismicity (red on Figs. 5 and 9).

Hypocentral depth starts to decrease after 70 days and the phase culminates in three events with highly similar waveforms at seismic stations in the entire Arctic region. These must occur at the same geographic location and image the same process. First arrival analysis of these three events implies that compressive stress is propagating from the earthquake source in all direc-

tions and indicates a strong volumetric component in the source as an explosion or expanding dike.

Phase B occurs just after the largest magnitude event and just before the percentage of double-couple components of high magnitudes drop permanently. We speculate that, when the largest event occurs in March 1999, stress drop opens the pathway for material from the upper mantle to penetrate the crust. In the following, the lateral distribution of events can narrow down so much that the waveforms of different events actually mirror the same process and the same location. A typical geological process that focuses energy into a single narrow pathway is volcanism.

Thus, we speculate that magma accumulates below the crust and only when the amount of buoyancy inside this accumulating body is high enough, stress intensity at the top reaches a threshold value. A dike can form and penetrates the crust. Pedersen et al. (2007) suggest that, in cases of high magmatic stress rate, i.e., in voluminous and rapid intrusions, high seismic energy release can be triggered.

Typical volcanic vents in the survey area and within the seismicity during phase B are the cones of a volcanic chain imaged by Sohn et al. (2008), which are related to explosive volcanism. Sohn et al. (2008) suggest deep gas accumulation and its rapid explosive discharge following models of Head and Wilson (2003) for these vents. Thus, it is likely that the seismic swarm with its high energy release could occur due to a rapid and contemporary magmatic intrusion that later delivers the magmatic ground mass for the discovered young Limu o Pele on the rim of these vents.

Seismicity during phase B rises (within 25 days) from the Moho to mid-crustal depths with an ascent velocity of 0.4 km/day or 0.46 cm/s (Fig. 9). We speculate that the shallower ascent phase to the seafloor produced only events of low magnitude and could not be imaged by globally monitorable seismicity. The red bars of median hypocentral depth in Fig. 9 assume a convex shape, indicating a sharp increase in ascent velocity which is typical for volcanic eruptions (Battaglia et al. 1999; Rivalta and Dahm 2006). The fastest ascent occurs at the end from 12.5 to 8 km depth in around 1 day, i.e., an increase of ascent velocity to 7.5 cm/s, which is typical for daily swarms at slow-spreading ridges, such as offshore North Iceland (Hensch et al. 2008), but on the lower end of rise velocities of mantle-derived magmatic dykes between 1 cm/s and 10 m/s globally (Rubin 1995).

4.3 Phase C

During mid-April or around day 110, the rate of seismicity decreases drastically (Tolstoy et al. 2001). We speculate that the area now adjusts to a changed stress field after the major phase of the volcanic eruption showing seismic events again scattered over a larger area, but mostly within a narrow band in depth. While Müller and Jokat (2000) attribute the nondouble-couple events of this phase to potential caldera-collapse phenomena, Tolstoy et al. (2001) point out that the creation of nondouble-couple focal mechanism occurs by distortion of focal mechanisms due to spatial heterogeneity within the source volume, for example, due to reduced seismic velocities in an area of partially molten or hot material, both of which are not excluded by our studies. The latter model would explain why earthquakes along the valley bounding faults show larger nondouble-couple events after a volcanic event. Additionally, it would fit observations that large delays for teleseismic arrivals occur in East Siberia and Alaska. They could well be the large-scale effect of the spatial change in the source volume.

However, in contrast to Tolstoy et al. (2001), we are confident that magnitude and nondouble-couple component are not linked with the increasing double-couple character for larger events (Table 4). Though seismicity stops suddenly at the end of September 2009 and the deep crust has potentially adjusted to the new stress situation, it seems likely that a strong eruption would leave remaining shallow heat centers or even open effusive vents for later years. Only locally installed seismometers would pick up the remaining seismic energy within the shallow crust or small seafloor explosions which have been described by Schlindwein et al. (2005).

5 Conclusions

The 1999 seismic swarm along Gakkel Ridge was analyzed for locations by optimizing the subsurface velocity models, calculating coherency of the waveforms of arrivals within the entire Arctic region, and verifying the double-difference behavior of earthquakes exhibiting similar waveforms. This lead to a list of overall station residuals during the entire swarm. Magnitude trends within the swarm, first arrival amplitudes, and nondouble-couple components of the moment tensor added to the following interpretation.

We find three events with almost equal waveforms and volumetric source component as crown witnesses for a volcanotectonic origin of the swarm and speculate that the location of the volcanic vent at the seafloor lies within the central rift valley at the southwestern edge or slightly outside a volcanic chain recently imaged from R/V Oden. We propose that opening of the vent occurred between 5 and 9 April 1999 when the source area narrows down laterally and an ascent of hypocenters can be observed through upper crustal material previously shattered by a tectonic earthquake sequence that occurred in the initial phase of the swarm and culminated in mid-March 1999.

Most of the seismicity is focused on the crust–mantle boundary that we imaged at 16 to 20 km depth and the neighboring layers in the lower crust and upper mantle and that we suggest to be the source area for magmatic material involved in the potential eruption. Our velocity model of the source area though sparsely sampled in the upper few kilometers shows a rather crystalline crust with no large velocity gradients and thus indicating next to no sedimentation. Heterogeneity of the source area, probably related to the eruption and post-eruptive phenomena, leads to high station residuals in the direction of Spitsbergen, Eastern Siberia, and Western Alaska.

Acknowledgements We thank the ISC, IRIS, NORSAR, and the Geological Survey of Canada for providing the used location and waveform data via their online access tools. We also want to thank Maya Tolstoy for providing their original dataset and Simone Cesca for providing some insight into moment tensor analysis. Last but not the least, we gratefully acknowledge the constructive feedback from H. Soosalu and an anonymous reviewer. This research was funded via the Emmy Noether programme by the Deutsche Forschungsgemeinschaft (Schl 853/1-1).

References

Baker ET, Edmonds HN, Michael PJ, Bach W, Dick HJB, Snow JE, Walker SL, Banerjee NR, Langmuir CH (2004) Hydrothermal venting in magma deserts: the ultraslow-spreading Gakkel and Southwest Indian Ridges. Geochem Geophys Geosyst 5:Q08002. doi:10.1029/2004GC000712

Battaglia J, Ferrazzini V, Staudacher T, Aki K, Cheminée J-L (1999) Pre-eruptive migration of earthquakes at the Piton de la Fournaise volcano (Réunion Island). Geophys J Int 161:549–558

Clague D, Paduan JB, Davis AS (2008) Widespread strombolian eruptions of mid-ocean ridge basalt. J Volcanol Geotherm Res 180:171–188

Coakley BJ, Cochran JR (1998) Gravity evidence of very thin crust at the Gakkel Ridge (Arctic Ocean). Earth Planet Sci Lett 162:81–95

Dahm T (2000) Numerical simulation of the propagation path and arrest of fluid-filled fractures in the earth. Geophys J Int 141:623–638

Daines MJ (2000) Migration of melt. In: Sigurdsson H, Houghton B, McNutt SR, Rymer H, Styx J (eds) Encyclopedia of volcanoes. Academic, New York

Dick HJB, Lin J, Schouten H (2003) An ultraslow-spreading class of ocean ridge. Nature 426:405–411

Dziak RP, Smith DK, Bohnenstiehl DR, Fox CG, Desbruyeres D, Matsumoto H, Tolstoy M, Fornari DJ (2004) Evidence of a recent magma dike intrusion at the slow spreading Lucky Strike segment, Mid-Atlantic Ridge. J Geophys Res 109:B12102. doi:10.1029/2004JB003141

Dziewonski AM, Anderson DL (1981) Preliminary reference Earth model. Phys Earth Planet Inter 25:297–356

Edmonds HN, Michael PJ, Baker ET, Connelly D, Snow JE, Langmuir CH, Dick HJB, Mühe R, German CR, Graham DW (2003) Discovery of abundant hydrothermal venting on the ultraslow-spreading Gakkel Ridge in the Arctic Ocean. Nature 421:252–256

Edwards MH, Kurras GJ, Tolstoy M, Bohnenstiehl DR, Coackley BJ, Cochran JR (2001) Evidence of recent volcanic activity on the ultraslow-spreading Gakkel Ridge. Nature 409:808–812

Einarsson P, Brandsdóttir B (1980) Seismological evidence for lateral magma intrusion during the July 1978 deflation of the Krafla volcano in NE-Iceland. J Geophys 47:160–165

Fox CG, Dziak RP (1998) Hydroacoustic detection of volcanic activity on the Gorda Ridge, February–March 1996. Deep-Sea Res II 45:2513–2530

Gibbons S (2006) On the identification and documentation of timing errors: an example at the KBS station, Spitsbergen. Seismol Res Lett 77:559–571

Head JW, Wilson L (2003) Deep pyroclastic eruptions, theory and predicted landforms and deposits. J Volcanol Geotherm Res 121:155–193

Hensch M, Riedel C, Reinhardt J, Dahm T (2008) Hypocenter migration of fluid-induced earthquake swarms in the Tjörnes Fracture Zone (North Iceland). Tectonophysics 447:80–94

Jokat W, Schmidt-Aursch M (2007) Geophysical characteristics of the ultra-slow spreading Gakkel Ridge, Arctic Ocean. Geophys J Int 168:983–998. doi:10.1111/j.1365-246X.2006.03278.x

Jost ML, Herrmann RB (1989) A students guide to and review of moment tensors. Seismol Res Lett 60:37–57

Kanamori H (1977) The energy release in great earthquakes. J Geophys Res 82:2981–2876

Kearey P, Vine FJ (1990) Global tectonics. Blackwell Scientific, Oxford

Kennett BLN, Engdahl ER (1991) Traveltimes for global earthquake location and phase identification. Geophys J Int 105:429–465

Kennett BLN, Engdahl ER, Buland R (1995) Constraints on seismic velocities in the Earth from travel times. Geophys J Int 122:108–124

Lee WHK, Lahr JC (1975) HYPO71 (revised): a computer program for determining hypocenter, magnitude and first motion pattern of local earthquakes. Open-file report, U.S. Geological Survey, pp 75–311

Lienert BR, Havskov J (1995) A computer program for locating earthquakes both locally and globally. Seismol Res Lett 66:26–36

Luckett R, Storchak D (2001) ISC loc software. Available at http://www.isc.ac.uk/code/iscloc

Maurer H, Deichmann N (1995) Microearthquake cluster detection based on waveform similarities, with an application to the western Swiss Alps. Geophys J Int 123:588–600

Michael PJ et al (2003) Magmatic and amagmatic seafloor generation at the ultra-slow Gakkel Ridge, Arctic Ocean. Nature 423:956–961

Müller C, Jokat W (2000) Seismic evidence for volcanic activity discovered in Central Arctic. EOS Trans AGU 81(24):265–269

Pedersen R, Sigmundsson F, Einarsson P (2007) Controlling factors on earthquake swarms associated with magmatic intrusions; constraints from Iceland. J Volcanol Geotherm Res 162:73–80

Ritzmann O, Maercklin N, Faleide JI, Bungum H, Mooney WD, Detweiler ST (2007) A three-dimensional geophysical model of the crust in the Barents Sea region: model construction and basement characterization. Geophys J Int 170(1):417–435. doi:10.1111/j.1365-246X.2007.03337.x

Rivalta E, Dahm T (2006) Acceleration of buoyancy-driven fractures and magmatic dikes beneath the free surface. Geophys J Int 166:1424–1439

Rubin AM (1995) Propagation of magma-filled cracks. Annu Rev Earth Planet Sci 23:287–336

Ruff LJ (2002) State of stress within the earth. In: Lee WHK, Kanamori H, Jennings PC, Kisslinger C (eds) International handbook of earthquake and engineering seismology, vol 81A. Academic, New York. ISBN: 0-12-440652-1

Schlindwein V, Müller C, Jokat W (2005) Seismoacoustic evidence for volcanic activity on the ultraslow-spreading Gakkel Ridge, Arctic Ocean. Geophys Res Lett 32:L1830. doi:10.1029/2005GL023767

Schlindwein V, Riedel C (2009) The 1999–2001 explosive volcanic episode on Gakkel Ridge, Arctic Ocean: reconstruction of the volcanic events from multidisciplinary observations. Geochem Geophys Geosyst (in press)

Schweitzer J (2001) HYPOSAT—an enhanced routine to locate seismic events. Pure Appl Geophys 158:277–289

Schweitzer J (2006) How can the ISC location procedures be improved? Phys Earth Planer Inter 158:19–26

Sohn RA et al (2008) Explosive volcanism on the ultraslow-spreading Gakkel Ridge, Arctic Ocean. Nature 453:1236–1238

Storchak DA (2006) Results of locating the IASPEI GT(0–5) reference events using the standard ISC procedures. Phys Earth Planet Inter 158:4–13

Tolstoy M, Bohnenstiehl DR, Edwards MH, Kurras GJ (2001) Seismic character of volcanic activity at the ultraslow-spreading Gakkel Ridge. Geology 29:1139–1142

Utsu T (2002) Relationship between magnitude scales. In: Lee WHK, Kanamori H, Jennings PC, Kisslinger C (eds) International handbook of earthquake and engineering seismology, vol 81A. Academic, New York. ISBN: 0-12-440652-1

Waldhauser F, Ellsworth WL (2000) A double-difference earthquake location algorithm: method and application to the Northern Hayward fault, California. Bull Seismol Soc Am 90:1353–1368

Wessel P, Smith WHF (1998) New, improved version of generic mapping tools released. EOS Trans 79:579

Wiemer S, McNutt S (1997) Variations in the magnitude–frequency distribution in two volcanic regions, Mt St Helens (Washington) and Mt. Spurr (Alaska). Geophys Res Lett 24:189–192